JOURNAL OF GEOPHYSICAL RESEARCH, VOL. 112, D11122, doi:10.1029/2006JD008230, 2007

The large-scale energy budget of the Arctic

Mark C. Serreze,[1] Andrew P. Barrett,[1] Andrew G. Slater,[1] Michael Steele,[2] Jinlun Zhang,[2] and Kevin E. Trenberth[3]

Received 7 November 2006; revised 23 February 2007; accepted 7 March 2007; published 14 June 2007.

[1] This paper synthesizes a variety of atmospheric and oceanic data to examine the large-scale energy budget of the Arctic. Assessment of the atmospheric budget relies primarily on the ERA-40 reanalysis. The seasonal cycles of vertically integrated atmospheric energy storage and the convergence of energy transport from ERA-40, as evaluated for the polar cap (defined by the 70°N latitude circle), in general compare well with realizations from the National Centers for Environmental Prediction/National Center for Atmospheric Research reanalysis over the period 1979–2001. However, shortcomings in top of atmosphere radiation, as compared to satellite data, and the net surface flux, contribute to large energy budget residuals in ERA-40. The seasonal cycle of atmospheric energy storage is strongly modulated by the net surface flux, which is also the primary driver of seasonal changes in heat storage within the Arctic Ocean. Averaged for an Arctic Ocean domain, the July net surface flux from ERA-40 of -100 W m^{-2} (i.e., into the ocean), associated with sea ice melt and oceanic sensible heat gain, exceeds the atmospheric energy transport convergence of 91 W m^{-2}. During winter (for which budget residuals are large), oceanic sensible heat loss and sea ice growth yield an upward surface flux of 50–60 W m^{-2}, complemented with an atmospheric energy convergence of 80–90 W m^{-2} to provide a net radiation loss to space of 175–180 W m^{-2}.

Citation: Serreze, M. C., A. P. Barrett, A. G. Slater, M. Steele, J. Zhang, and K. E. Trenberth (2007), The large-scale energy budget of the Arctic, *J. Geophys. Res.*, *112*, D11122, doi:10.1029/2006JD008230.

1. Introduction

[2] The Arctic is a complex system, characterized by intimate couplings between its atmosphere, ocean, lands, and lower latitude forcing operating on a spectrum of temporal and spatial scales. However, if the system is pared down to the essential components of its large-scale energy budget, describing the relationships between horizontal atmospheric and oceanic transports, net radiation at the top of the atmosphere, and net heat transfers between the atmospheric and subsurface reservoirs, it has an elegant simplicity.

[3] In 1988, *Nakamura and Oort* [1988] examined the basic energy budgets of the north and south polar caps (the regions poleward of 70°N and 70°S, respectively). While information on some of the budget terms was limited at that time, the paper provided a valuable view of the primary interactions that shape the observed character of the Arctic. Since that study, and subsequent efforts by *Overland and Turet* [1994] and others, a wealth of new information has become available.

[4] The present paper has two primary objectives. The first is to evaluate the atmospheric energy budget of the Arctic as represented by atmospheric reanalyses, emphasizing products from the European Centre for Medium Range Weather Forecasts (ECMWF) ERA-40 effort. This includes (1) comparisons between ERA-40 and the National Centers for Environmental Prediction/National Center for Atmospheric Research reanalysis (NCEP/NCAR, hereafter NRA) for atmospheric energy storage and energy transport convergence, focusing on the north polar cap, and (2) an assessment of shortcomings in the ERA-40 budget. The second objective is to combine ERA-40 data with estimates of oceanic sensible heat content, sensible heat transport, and sea ice transport to link the energy budgets of the Arctic Ocean and its overlying atmosphere with radiation to space. The two domains are shown in Figure 1.

[5] This paper complements a new analysis of the Arctic's large-scale freshwater budget [*Serreze et al.*, 2007], a recent study of the atmospheric heat and water budgets for the north polar cap by *Semmler et al.* [2005], using output from a regional climate model, and existing global energy budget studies [e.g., *Trenberth and Caron*, 2001; *Trenberth et al.*, 2001; *Trenberth and Stepaniak*, 2003, 2004].

[6] Section 2 discusses the budget framework and study domains, whereas section 3 describes the data sources. Section 4 examines the atmospheric energy budget of the polar cap region, with foci on the annual mean and seasonal cycle, spatial patterns of key components, and selected time series. In section 5, attention turns to linking the energy

[1]Cooperative Institute for Research in Environmental Sciences, University of Colorado, Boulder, Colorado, USA.
[2]Applied Physics Laboratory, Polar Science Center, University of Washington, Seattle, Washington, USA.
[3]National Center for Atmospheric Research, Boulder, Colorado, USA.

0148-0227/07/2006JD008230$09.00

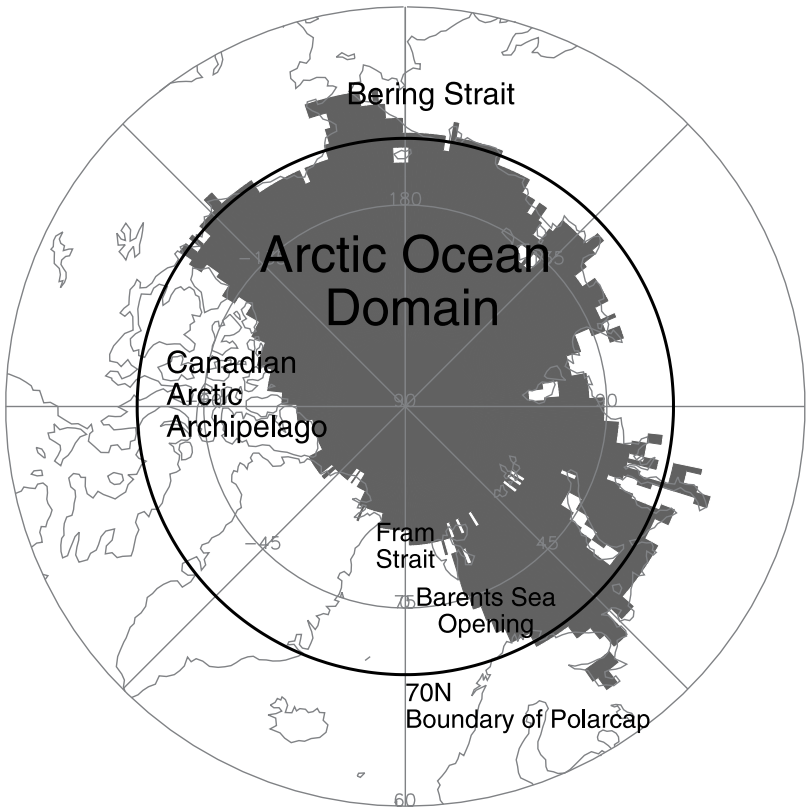

Figure 1. Polar cap and Arctic Ocean domains used in this study. Major geographic features referred to in the text are also indicated.

budgets of the atmosphere and Arctic Ocean. Results are synthesized in section 6.

2. Framework and Study Domains

2.1. Budget Framework

[7] Following the works of *Nakamura and Oort* [1988] and *Trenberth* [1997], consider the energy budget of an atmospheric column, extending from the surface to the top of the atmosphere. Building on this conceptual framework, a subsurface column extends from the surface downward. The budget of the atmospheric column can be expressed as:

$$\partial A_E/\partial t = -\nabla \bullet \mathbf{F}_A + R_{top} + F_{sfc} \quad (1)$$

where the time change (tendency) of atmospheric energy storage A_E in the column represents the sum of the convergence of atmospheric energy transport ($-\nabla \bullet \mathbf{F}_A$), the net radiation at the top of the atmosphere (R_{top}, positive downward), and the net heat flux at the Earth's surface (F_{sfc}, positive upward). If the sum of the three terms on the right is positive, the atmospheric column gains energy. If their sum is negative, the column loses energy.

[8] The tendency in atmospheric energy storage is represented as

$$\partial A_E/\partial t = \partial/\partial t\, 1/g \int_o^{ps} \left(c_p T + k + Lq + \Phi_s\right) dp \quad (2)$$

where p is pressure, c_p is the specific heat of the atmosphere at a constant pressure (1005.7 J K^{-1} kg^{-1}) [*AMS*, 2000], T is temperature in Kelvin, k is the kinetic energy, L is the latent heat of evaporation (2.501 $\times$ 10^6 J kg^{-1}), q is the specific humidity (the ratio of the mass of water vapor in a sample to the total mass of air in a sample), g is the gravitational acceleration (approximately 9.81 m s^{-2}), and Φ_s is the surface geopotential. The latter is not a function of pressure [e.g., see *Trenberth et al.*, 2001]. Each of the terms in parentheses has units of Joules per kilogram (J kg^{-1}), i.e., energy per unit mass, whereas the terms k and Φ_s have the more obvious units of m^2 s^{-2}; this is the same. Integration by dp and division by g yields units of J m^{-2}. Taking the tendency results in W m^{-2}. In a steady state, the tendency in storage would be zero for the long-term annual mean.

[9] In this framework, liquid water is taken to be the zero latent heat state. This means that snowfall would appear as an energy gain in the atmosphere and an energy loss at the surface. The latent heat content of the atmosphere also ignores liquid water or ice in the atmosphere itself.

[10] The convergence of atmospheric transport

$$-\nabla \bullet \mathbf{F}_A = -\nabla \bullet 1/g \int_o^{ps} \left(c_p T + \Phi + Lq + k\right)\mathbf{v}\, dp \quad (3)$$

where $\mathbf{v}$ is the horizontal wind vector. The dry static energy is represented by $c_pT + \Phi$; moist static energy is $c_pT + \Phi + Lq$. Kinetic energy is typically a small component of the energy budget and was ignored by *Nakamura and Oort* [1988].

[11] R_{top}, the net radiation at the top of atmosphere (TOA), represents the difference between the TOA net solar

radiation and longwave emission, and is measured by satellite as part of the Earth radiation budget.

[12] The net surface heat flux is the net heat transfer between the atmospheric column and the subsurface column extending from the surface downward. It can be expressed as

$$F_{\mathrm{sfc}} = R_{\mathrm{sfc}} + Q_{\mathrm{H}} + Q_{\mathrm{E}} \quad (4)$$

where R_{sfc} is the net radiation at the surface, and Q_{H} and Q_{E} are the turbulent sensible and latent heat fluxes (all three terms are positive upward). If the sum is negative, there is a net heat flux from the atmospheric column into the subsurface column. If the sum is positive, the opposite holds.

[13] The energy budget of the subsurface column, if represented by ocean, is approximately

$$\partial O_{\mathrm{E}}/\partial t = \partial/\partial t(L_{\mathrm{i}} + S_{\mathrm{o}} + S_{\mathrm{i}}) = -\nabla \bullet \mathbf{F}_{\mathrm{o}} + \nabla \bullet \mathbf{F}_{\mathrm{i}} - F_{\mathrm{sfc}} \quad (5)$$

which states that the tendency in energy storage of the ocean $\partial O_{\mathrm{E}}/\partial t$ can be broken down into changes in latent heat storage as floating sea ice and any overlying snow cover (L_{i}) changes in sensible heat storage of the ocean water (S_{o}) and changes in sensible heat storage as sea ice (S_{i}). The tendency in oceanic energy storage is in turn equal to the sum of the net surface heat flux, the horizontal convergence of the oceanic sensible heat flux ($\mathbf{F}_{\mathrm{o}}$), and the horizontal divergence of the latent heat flux as sea ice ($\mathbf{F}_{\mathrm{i}}$). The combination of the latter two is the oceanic equivalent of the atmospheric transport in equation (1). $\nabla \bullet \mathbf{F}_{\mathrm{i}}$ represents heat exchanges associated with the divergence of sea ice by winds and ocean currents. A given mass of ice has a lower energy content than a given mass of water at the same temperature. Assuming that a net export (divergence) of sea ice from a column is replaced by the same mass of water at the same temperature, there is an effective increase in the heat content of the subsurface column. The sea ice terms in equation (5) could include contributions by icebergs. Several small terms are ignored, including the sensible heat of the ice transport, kinetic energy changes in the ocean, and sensible heat transports associated with river discharge into the ocean.

[14] For terrestrial (T) regions, the energy budget of the subsurface column is approximately:

$$\partial T_{\mathrm{E}}/\partial t = \partial/\partial t(L_{\mathrm{T}} + S_{\mathrm{T}}) = -F_{\mathrm{sfc}} \quad (6)$$

where L_{T} and S_{T} are the terrestrial latent and sensible heat storages, respectively. Equation (6) assumes that lateral heat transport divergences are small and can be ignored, such that the tendency in terrestrial heat storage is due only to the net surface flux. It is recognized, however, that lateral heat transports by rivers can be locally significant [*Su et al.*, 2006].

[15] *Nakamura and Oort* [1988] argued that when considering the polar cap domain as a whole, $-\nabla \bullet \mathbf{F}_{\mathrm{o}}$ and $\nabla \bullet \mathbf{F}_{\mathrm{i}}$ in equation (5) are both small and fairly steady through the year, and that L_{T} and S_{T} from equation (6) are also quite small. Consequently, they concluded that the change in energy of the subsurface for the polar cap as a whole is governed primarily by the net surface flux, approximately divided between changes in sensible and latent heat storage of the ocean (the latter associated with sea ice growth and melt). These assumptions will be explored later.

2.2. The Polar Cap and Arctic Ocean Domains

[16] The polar cap domain (area of 15.4×10^6 km^2, 72% represented by ocean, Figure 1) facilitates interpreting longitudinal variations in meridional atmospheric energy transports across its boundary. It also fosters comparisons with previous studies for this domain [e.g., *Nakamura and Oort*, 1988; *Overland and Turet*, 1994; *Rogers et al.*, 2001; *Trenberth and Stepaniak*, 2003; *Semmler et al.*, 2005].

[17] The Arctic Ocean domain (Figure 1, area of 9.56×106 km^2) is the same as used by *Serreze et al.* [2007] in their companion study of the Arctic freshwater budget. The boundary between the Arctic and Pacific oceans is the Bering Strait, between Alaska and eastern Russia. Boundaries between the Arctic Ocean and Atlantic are Fram Strait, between northern Greenland and Svalbard, and the passage between Svalbard and northern Scandinavia (the Barents Sea opening). The other Atlantic connection is through the channels of the Canadian Arctic Archipelago. This domain is well suited for linking the atmospheric and ocean energy budgets as (1) sufficient hydrographic data are available within the domain to assess the annual cycle in oceanic heat storage, (2) models and observations provide estimates of oceanic heat fluxes through the major straits, and (3) nearly all of the divergence of the latent heat flux in the form of snow and ice [equation (6)] represents the transport of sea ice out of the Arctic through Fram Strait.

3. Primary Data Sources

3.1. Atmospheric Reanalyses

[18] Assessments of the atmospheric energy budget rely primarily on data from the ERA-40 reanalysis, but comparisons are made with NRA. Atmospheric reanalysis is a retrospective form of numerical weather prediction whereby time series of analyzed atmospheric fields and modeled fields are compiled using fixed versions of the forecast/data assimilation system. Analyzed fields, such as tropospheric pressure heights, winds, humidity, and temperature, blend a short-term atmospheric forecast with observations. These are generally the most reliable. Fields such as TOA radiation and terms of the surface energy budget (from which the net surface flux can be computed) are less reliable because they are not influenced in the reanalysis by direct observations of those variables. In an operational setting, the forecast/data assimilation system is constantly refined to improve forecast skill, which can lead to nonclimatic jumps and trends in archived fields. By using fixed systems, archives from reanalysis are more consistent, but inconsistencies are still present because of changes in observing networks (for example, rawinsonde and satellite databases).

[19] Data from the NRA [*Kalnay et al.*, 1996; *Kistler et al.*, 2001] have been widely used in Arctic studies [e.g., *Serreze et al.*, 1998, 2001, 2003; *Cullather et al.*, 2000; *Serreze and Hurst*, 2000; *Rogers et al.*, 2001]. The NRA model has a horizontal resolution of T-62 with 28 vertical levels. Fields are available every 6 hours from 1948 onward.

[20] ERA-40, with a horizontal resolution of T-159 and 60 levels in the vertical, can be viewed as a next-generation reanalysis. Arctic performance is a subject of ongoing evaluation [e.g., *Bromwich et al.*, 2002; *Serreze et al.*, 2005, 2007]. Six-hourly fields from 1957 to July 2002 are available at NCAR on a grid with an approximate 125-km

spacing (the N-80 grid). ECMWF has no plans to extend the ERA-40 reanalysis to more recent years. ERA-40 makes extensive use of multichannel satellite radiances. A significant difference with respect to the earlier ECMWF ERA-15 effort (1979–1993) and NRA is the assimilation of raw satellite radiances as opposed to retrieved properties. This avoids inconsistencies due to changes introduced in satellite data processing over the years. There are numerous improvements in the land surface scheme, many driven by high-latitude concerns. ERA-40 also features improved sea surface temperature and sea ice boundary fields, and, unlike NRA, includes increasing greenhouse gases in the atmosphere. The study by *Uppala et al.* [2005] provides an overview.

[21] The terms of A_E and $-\nabla \bullet \mathbf{F}_A$ [equations (2) and (3)] represent vertical integrals of analyzed fields. Vertical integrals represent standard fields in the ERA-40 archives at NCAR, but the atmospheric transports require mass correction (discussed shortly). Vertical integrals from NRA for 1979 through 2005, with mass corrections to the transports, have been assembled by *Trenberth et al.* [2001] at T42 on a 128 × 64 (latitude by longitude) Gaussian grid (http://www.cgd.ucar.edu/cas/catalog/newbudgets/index.html).

[22] ERA-40 is used to assess all components of the atmospheric budget over the period 1979–2001. Fields since 1979 are more reliable than those for earlier years because of the availability of extensive satellite data for assimilation. Comparisons between ERA-40 and NRA for atmospheric transports, energy storages, and tendencies focus on this common period. Terms averaged over the polar cap and Arctic Ocean domain are obtained by averaging the grid cell values enclosed by the domain boundaries, with weights to account for latitude changes in grid cell size. The domain-averaged convergence of the atmospheric energy transport is equivalent to integrating the meridional flux around the 70°N circle.

[23] Emphasis on newer ERA-40 system recognizes that terms of the Arctic surface energy budget in NRA contain extreme biases. For example, downwelling shortwave radiation fluxes over the Arctic Ocean in summer may be 60 W m^{-2} too high [*Serreze et al.*, 1998]. Land-surface evaporation rates in NRA are also excessive [*Serreze and Hurst*, 2000]. However, as will be seen, there are shortcomings in the ERA-40 TOA radiation, as well as in the net surface flux.

3.2. Mass Corrections to Atmospheric Transports

[24] The analyzed fields from reanalysis are not in mass balance. To provide meaningful results, the transports require mass correction [*Trenberth*, 1997; *Trenberth et al.*, 2001]. Trenberth et al. at NCAR have already applied these to the NRA products over the period 1979–2005. The same techniques are applied to ERA-40. The first step is to derive a mass budget residual (R) at each grid cell, which is an estimate of the degree of atmospheric mass balance:

$$R = \partial p_s/\partial t + \nabla \bullet \left(\int_o^{ps} (u)\mathrm{d}p, \int_o^{ps} (v)\mathrm{d}p \right) - g(E - P) \quad (7)$$

The terms on the right are the tendency in surface pressure (p_s), the vertically integrated mass flux divergence, and the difference between evaporation (E) and precipitation (P) adjusted by g. One then defines a potential function X as:

$$R = \nabla^2 X \quad (8)$$

[25] A mass correction that minimizes the mass balance residual is obtained by applying a barotropic correction to the vertically and monthly averaged zonal and meridional winds (U_c, V_c):

$$(U_c, V_c) = \nabla X/(P_s - gP_w) \quad (9)$$

where P_w is precipitable water. These corrections are then applied to the vertically integrated zonal and meridional transports, which are then used to calculate the convergences.

3.3. Satellite Data

[26] The TOA radiation budget from ERA-40 is compared to estimates from the Earth Radiation Budget Experiment (ERBE) data set and other sources. The revised ERBE record, available for February 1985 to April 1989, combines information from three satellites (see the work of *Trenberth and Solomon* [1994] and the above web site for the NRA budget products). *Allan et al.* [2004] compared the ERA-40 TOA radiation budget with ERBE data along with information from the Scanner for Radiation Budget (ScaRaB) instrument (1994–1995) and the Clouds and the Earth's Radiation Energy Systems (CERES) product from the Tropical Rainfall Measurement Mission satellite (January-August 1998). The study by *Kato et al.* [2006] also provides a recent analysis of the Arctic radiation budget using CERES and ERBE. Estimates of planetary albedo are also available from the Arctic Polar Pathfinder (APP-x) product based on Advanced Very High Resolution Radiometer (AVHRR) data [*Key and Intrieri*, 2000; *Key et al.*, 2001].

3.4. Terms of the Ocean Energy Budget

[27] An annual cycle of oceanic sensible heat content for the Arctic Ocean domain is compiled from the University of Washington Polar Science Center Hydrographic Climatology (PHC; http://psc.apl.washington.edu/Climatology.html). The PHC uses optimal interpolation to combine data from the 1998 version of the World Ocean Atlas [*Antonov et al.*, 1998; *Boyer et al.*, 1998] with records from the regional Arctic Ocean Atlas [*EWG*, 1997, 1998] and Bedford Institute of Oceanography. The work of *Steele et al.* [2001] provides an overview of Version 2.0. The PHC is only a long-term climatology, with many of the measurements collected in the 1970s. Most are from spring and summer.

[28] The study by *Vinje et al.* [1998] provides estimates of monthly sea ice volume transport through Fram Strait for August 1990 through July 1996. These combine information on ice thickness across the strait from upward looking sonar (ULS), ice velocity from drifting buoys, and the difference in sea level pressure (SLP) between Fram Strait and the central core of the northern North Atlantic trough, as well as the width of the ice stream. The SLP gradient is an index of the wind-driven component of the ice transport. Monthly means from the longer record assembled by *Vinje* [2001] are very similar. An ice density of 900 kg m^{-3} is assumed. Sea ice transports through the other straits

Table 1. Monthly and Annual Mean Components of the Atmospheric Energy Budget of the North Polar Cap From ERA-40 and Other Sources

	Fluxes and Storage Changes, W m^{-2}					
Month	$\partial A_E/\partial t$[a]	R_{top}[b]	$-\nabla \bullet \mathbf{F}_A$[c]	F_{sfc}	Plan. Albedo[d]	Res.[e]
January	−2 (−1)	−175 [−11]	108 (117)	56	–	−9
February	5 (5)	−171 [−10]	112 (128)	51	–	−13
March	12 (12)	−143 [−1]	110 (121)	40	0.71	−5
April	25 (25)	−88 [11]	92 (102)	17	0.66	−4
May	21 (21)	−27 [26]	66 (77)	−18	0.64	0
June	18 (18)	23 [18]	89 (78)	−70	0.54	24
July	1 (−1)	11 [9]	94 (81)	−85	0.45	19
August	−17 (−16)	−66 [1]	98 (91)	−39	0.48	10
September	−27 (−26)	−145 [−5]	106 (104)	17	0.55	5
October	−22 (−22)	−183 [−9]	114 (108)	53	–	6
November	−11 (−12)	−184 [−12]	105 (114)	55	–	−13
December	−3 (−4)	−178 [−12]	111 (115)	58	–	−6
Mean	0 (0)	−110 [1]	100 (103)	11	–	−1

[a]Values in parentheses are from NRA.
[b]Values in brackets are ERA-40 minus ERBE for the common record period February 1985 to April 1989.
[c]Values in parentheses are from NRA.
[d]Planetary albedo from the AVHRR Polar Pathfinder Project.
[e]Energy budget residual in ERA-40 calculated as $R_{top} - \nabla \bullet \mathbf{F}_A + F_{sf} = \partial A_E/\partial t$.

defining the Arctic Ocean domain are quite small, except perhaps for some anomalous years [*Kwok et al.*, 2005].

[29] For oceanic sensible heat transports, primary use is made of output from the global Parallel Ice-Ocean Model (PIOM), which couples the Parallel Ocean Program model developed at the Los Alamos National Laboratory with a multicategory thickness and enthalpy distribution sea ice model [*Zhang and Rothrock*, 2003; *Zhang*, 2005]. PIOM is driven with daily NRA forcings, which include 10-m winds, surface air temperature, specific humidity, radiation fluxes, and evaporation. As noted above, some of these forcings are known to have strong biases. Ocean temperature and salinity are initialized to observed climatology. Model spin-up consists of an integration of 30 years using 1948 forcings repeatedly. After spin-up, the model simulates the period 1948–2003. The present study uses output for 1955–2003 from the study by *Zhang* [2005]. Comparisons are made with results from coupled ice-ocean model simulations described by *Maslowski et al.* [2004], forced by ECMWF data. The studies of *Hopkins* [1991], *Rudels* [1987] (both from Table 2a of the summary by *Simonsen and Haugen* [1996]), and *Schauer et al.* [2004] provide observationally based estimates to complement the model results.

4. Atmospheric Energy Budget of the Polar Cap

4.1. Annual Means and Annual Cycle

[30] Table 1 gives annual averages and monthly means of the basic atmospheric budget terms [equation (1)] for the polar cap (the region north of 70°N) in W m^{-2}. Monthly atmospheric transports and tendencies of atmospheric energy are given for both ERA-40 and NRA. The tendencies for both reanalyses are calculated following the study by *Trenberth et al.* [2001]. The energy content at the beginning of a month (BEG) was obtained by averaging the energy content at 18Z of the last day of the previous month and 00Z of the first day of the given month. The energy content at the end of the month (END) was obtained from averaging 18Z of the last day of the given month and 00Z of the first day of the next month. The monthly tendency is then (END − BEG) / (N * 86,400), where N is the number of days in the month and 86,400 is the number of seconds in a day. Along with R_{top} from ERA-40, the ERA-40 minus ERBE difference is provided over the common period of coverage (February 1985 to April 1989). Planetary albedo from the APP-x data set is listed for months with a significant solar flux. Also given is the residual in the ERA-40 energy budget. This indicates the degree of closure (or lack thereof) in the budget averaged over 1979–2001. With perfect closure, the residual would be zero.

[31] Looking first at the annual means of atmospheric transport, it is encouraging that the mass-adjusted value of 100 W m^{-2} from ERA-40 is quite close to the value of 103 W m^{-2} from NRA. On the basis of simulations with REMO 5.1 over nearly the same period 1979–2000, *Semmler et al.* [2005] report 99 W m^{-2}. Their simulation was driven at the lateral boundaries using data from ERA-15 and (for 1994 onward) operational fields from ECMWF. The annual transport from the work of *Nakamura and Oort* [1988], based on a 10-year data set (November 1963–1973) compiled by the Geophysical Fluid Dynamics Laboratory (GFDL), is 98 W m^{-2}. From an expanded GFDL data set (November 1964–1989), *Overland and Turet* [1994] also report 103 W m^{-2}. With recognition that these estimates are based on different periods and data sources, the annual value in $-\nabla \bullet \mathbf{F}_A$ seems well constrained. The annual TOA radiation deficit in ERA-40 is −110 W m^{-2} compared to −104 W m^{-2} from the REMO 5.1 simulations. Over their common time period, annual means from ERA-40 and ERBE are nearly identical.

[32] ERA-40 depicts a mean annual upward net surface flux (a heat transfer from the subsurface column to the atmospheric column) of 11 W m^{-2}. *Nakamura and Oort* [1988] estimated a much smaller value of 2.4 W m^{-2}. Theirs was calculated as a residual from the atmospheric transport based on the GFDL data set and R_{top} based on data from Earth-orbiting satellites between the years 1966 and 1977. The REMO 5.1 annual value of 6 W m^{-2} falls roughly in the middle. These differences can be important. For example, a net surface flux of 1 W m^{-2} over a year is equivalent to melting approximately 0.1 m of sea ice at its melting point. The difference in the net surface flux between ERA-40 and REMO 5.1, taken over a year, hence represents roughly half a meter of ice. In a steady state climate, the positive net surface flux in the long-term annual mean would have to be balanced by oceanic sensible heat and sea ice transports [equation (5)]. While global warming invalidates the assumption of steady state, results for the Arctic Ocean domain (discussed later) argue that the ERA-40 annual net surface flux is too large.

[33] The range between estimates of the terms can be larger for individual months or seasons. For example, differences in atmospheric transport between ERA-40 and NRA are 16 W m^{-2} in February, whereas the May minimum of 66 W m^{-2} in ERA-40 is 11 W m^{-2} short of the corresponding NRA value. Monthly atmospheric energy tendencies from the two reanalyses are within 1–2 W m^{-2} of each other. Our winter and summer averages of 55 and −65 W m^{-2} for the

net surface flux compare well to corresponding values from REMO 5.1 [*Semmler et al.*, 2005] of 52 and −67 W m^{-2}. On the other hand, there can be large differences in the monthly R_{top} from ERA-40 and ERBE over their common period of record. In autumn and winter, R_{top} in ERA-40 is too negative compared to ERBE, whereas for spring and summer, the opposite holds. In May, the two estimates differ by 26 W m^{-2}.

[34] This brings us to the energy budget residuals in ERA-40. In the annual mean, the ERA-40 atmospheric energy budget, after applying mass corrections to the atmospheric transports, is almost closed. However, this is the result of compensating positive and negative residuals for individual months. Spatial fields of residuals for January and July down to 60°N are shown in Figure 2. Following the work of *Trenberth and Solomon* [1993], these fields were truncated from T159 resolution to T42 using a tapered weighting function to remove excessive (and extraneous) noise that exists at higher wave numbers. The basic conclusions are that the residuals may be very large depending on location, and their spatial structure varies seasonally. Negative residuals dominate the Barents, Kara, and Laptev seas in all months. The extent of negative residuals (energy deficits) is large in January, covering much of the Arctic Ocean and land areas. Consistent with Table 1, July shows a majority of positive residuals (energy surpluses) over the polar cap region. Given that the atmospheric transports have been mass corrected, one is led to conclude that the imbalances arise largely from the ERA-40 TOA radiation and net surface fluxes.

[35] For most of the year, the Arctic land is largely covered by high albedo snow (>0.70), and the albedo of sea ice is high even in summer (0.50–0.60). Snow and ice albedo are difficult to parameterize, and even small errors could substantially impact the TOA radiation budget, as well as the net surface flux. Furthermore, the Arctic is cloudy throughout the year, but especially in summer over the ocean when there is extensive low level stratus [*Herman and Goody*, 1976; *Beesley and Moritz*, 1999], for which both shortwave and longwave radiative properties are still not well understood. There may also be competing effects between temporal changes in surface albedo and in clouds [*Kato et al.*, 2006].

[36] *Yang et al.* [1999] and *Allan et al.* [2004] documented problems in R_{top} for both NRA and ERA-40. *Allan et al.* [2004] compared the ERA-40 TOA radiation budget with ERBE data along with information from the ScaRaB instrument (1994–1995) and CERES product (January-August 1998). Evaluated over common periods of record, the TOA radiation budget in ERA-40 was found to be inferior to NCEP. *Allan et al.* [2004] emphasized inaccurate radiative properties of clouds (rather than problems in cloud fraction) and (for high latitude lands) underestimation of surface albedo in ERA-40. The latter is associated with overestimates of both absorbed solar radiation (ASR) and outgoing longwave radiation (OLR). Their high-latitude comparisons, however, are primarily limited to results from the short ScaRab record: The ERBE comparisons use only data from the Earth Radiation Budget Satellite for 60°N to 60°S, whereas the CERES data only span 40°N to 40°S. They did not address seasonality.

[37] The monthly ERA-40 minus ERBE differences shown in Table 1 are computed using the revised ERBE record which combines information from three satellites. *Trenberth and Solomon* [1994] estimated a root mean square error of the ERBE fluxes of 7.8 W m^{-2} for the three-satellite combination. There is similarity between the seasonal structure of these differences and the ERA-40 energy budget residuals (last column of Table 1). This also holds when the ERA-40 residuals are calculated for the ERBE period.

[38] To the extent that the revised ERBE record can be used to validate ERA-40, the negative differences between ERA-40 and ERBE in winter point to excessive OLR (solar radiation is small or absent in winter). While deferring additional evaluation to a future study, it is likely relevant with respect to OLR that the vertically integrated sensible heat storage in ERA-40 is high relative to NRA for all months (see section 4.4). Positive ERA-40 minus ERBE differences for spring and summer suggest a contribution from overly low albedo (as suggested by the study of Allan et al.). The differences in Table 1 are largest for May, when high albedo is coupled with a fairly large solar flux. However, the study of *Kato et al.* [2006] points to shortcomings in ERBE. Their study focused on CERES depictions of TOA fluxes and planetary albedo for the region 60–90°N. As part of the effort, comparisons were made with an ERBE-like product that applies the ERBE algorithms to CERES radiances. Errors in TOA radiances from the CERES instruments are smaller than those in ERBE largely because of better scene identification and better angular distribution models. As averaged for the period March 2000 through February 2004, the CERES albedo of 0.469 is somewhat lower that the ERBE-like value of 0.487. The annual net allwave TOA flux from the ERBE-like product is about 5 W m^{-2} more negative than the CERES value, which seems to be largely determined by the albedo difference. The CERES data suggest that the spring and summer TOA budget in ERA-40 may not be as bad as indicated in Table 1.

[39] With these caveats in mind, we step through the annual cycle of the atmospheric energy budget from ERA-40. To complement Table 1, Figure 3 gives graphical representations from ERA-40 of (1) the four primary atmospheric terms, (2) TOA radiation budget components, (3) atmospheric transport and its latent heat and dry static energy components, and (4) terms of the surface budget.

[40] According to ERA-40, there is a net loss of energy from the atmospheric column in August of −17 W m^{-2}. The net loss is largest in September (−27 W m^{-2}) and becomes less negative through the winter (Figure 3a). The atmosphere begins to gain energy in February. The net energy gain increases during spring to a maximum of +25 W m^{-2} in April. Essentially, steady state conditions characterize July. This annual cycle, which is similar to that computed by *Nakamura and Oort* [1988], will be reflected in the changing magnitude and sign of the vertical and horizontal fluxes.

[41] During autumn, there is a growing TOA net radiation deficit as net solar radiation declines while net longwave losses remain large (Figure 3b). The autumn decline in the solar flux and hence its contribution to cooling of the atmospheric column is greater in high as compared to middle latitudes. While this fosters an increase in the atmospheric transport, the increase with respect to summer is modest. This can be understood from the net surface flux, which turns positive, also adding energy to the atmospheric

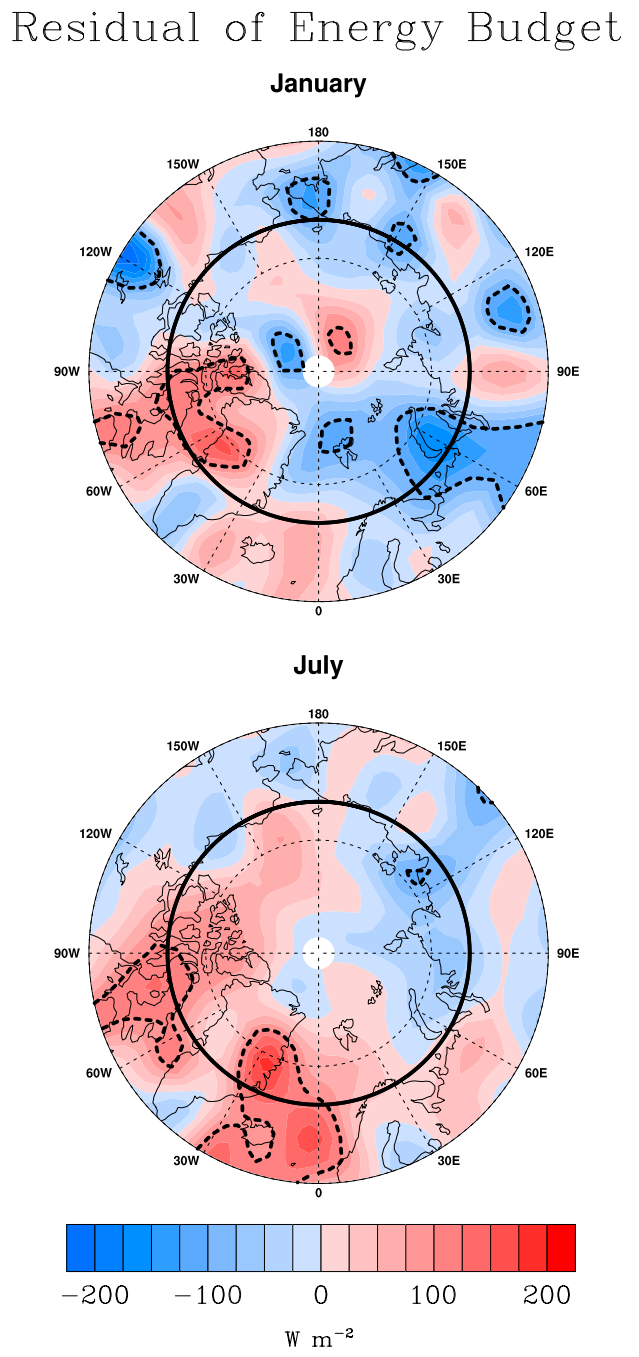

Figure 2. Maps of the energy budget residual from ERA-40 for January and July extending down to 60°N. The 70°N latitude circle is indicated in bold. Contours for −100 and 100 W m^{-2} are shown as dashed lines.

column. Hence although the atmosphere is losing energy strongly in autumn, fundamentally because of the declining solar flux, attendant increases in both F_{sfc} and the atmospheric transport act as "brakes" on the system. Put differently, the atmosphere loses energy at a slower rate than one would expect simply from the declining solar flux.

[42] The atmosphere continues to lose energy through January, but at a slower rate than for autumn. The net solar flux is essentially zero. In January, the TOA longwave loss is almost balanced by the combination of atmospheric transport and F_{sfc}.

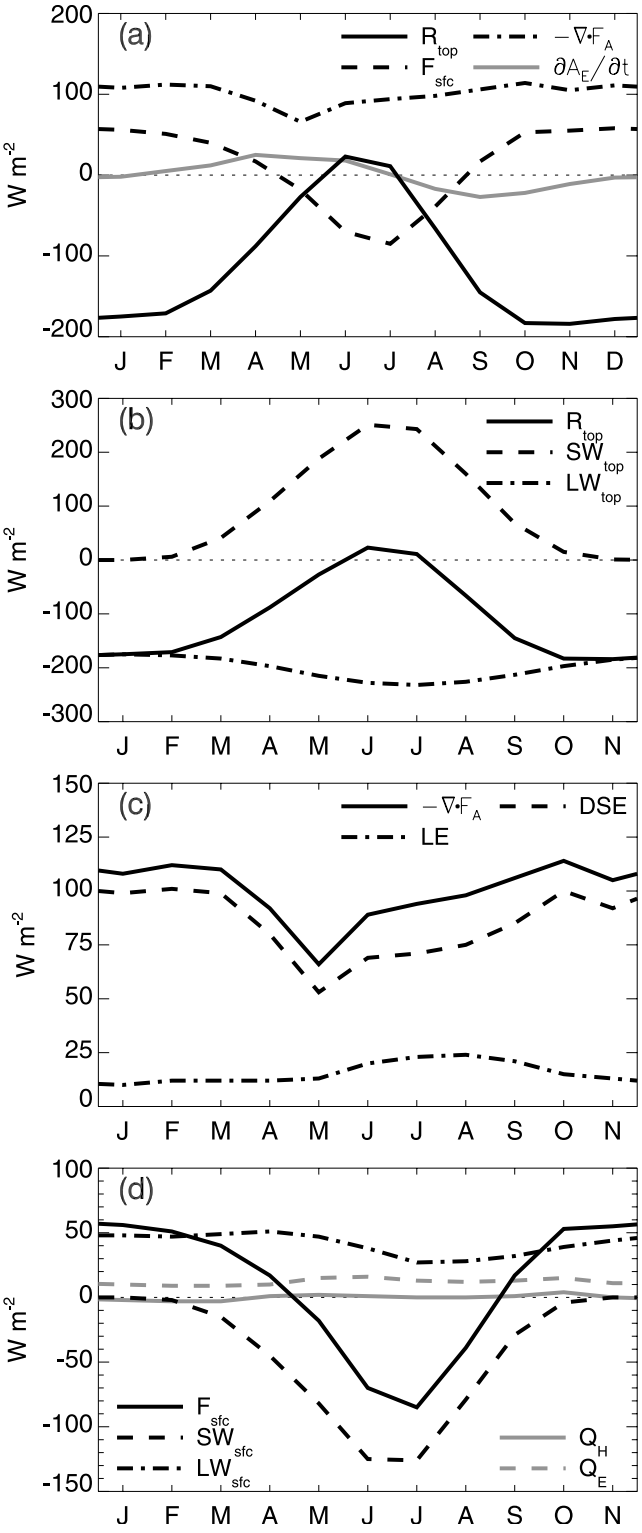

Figure 3. Annual cycles from ERA-40 of terms of: (a) the atmospheric energy budget; (b) the TOA radiation budget (R_{top}) with SW_{top} and LW_{top} being shortwave and longwave components, respectively; (c) atmospheric transport, with DSE and LE being dry static energy and latent heat energy, respectively (the small kinetic energy term is not shown); (d) the surface energy budget, with SW_{sfc} and LW_{sfc} being shortwave and longwave radiation components, and Q_H and Q_E being the turbulent sensible and latent heat fluxes, respectively.

[43] Spring approaches and the atmosphere begins to gain energy. The positive tendency in atmospheric energy storage is largest in April and May due primarily to the large input of solar radiation which strongly reduces the TOA net radiative loss (R_{top}). However, atmospheric energy gain is modulated by the high planetary albedo associated with sea ice, snow cover, and cloud cover. In addition, the sign of the net surface flux changes from positive to negative. Atmospheric transport declines sharply to a minimum in May. The continued positive change in atmospheric energy content during June would be much larger than indicated in Table 1 if not for the strong losses associated with the net surface flux (a transfer of heat from the atmospheric into the subsurface column).

[44] According to ERA-40, the net surface flux during June and July is almost as large as the atmospheric transport. As cloud cover over the Arctic Ocean is at its maximum in summer, mostly extensive low-level stratus, the low planetary albedo in July is primarily due to extensive open water and snow-free land. By August, TOA net solar radiation has declined from its June peak, and TOA net radiation has turned negative. The net surface flux for August is also still negative. Both processes contribute to a loss of atmospheric energy, with the atmospheric transport acting to decrease the rate of loss.

[45] Atmospheric transport is dominated by dry static energy (sensible heat plus geopotential). The annual cycle in the much smaller latent heat term (Figure 3c) is, by contrast, characterized by a late summer to early autumn peak, as it follows the higher temperatures and increased water holding capacity of the atmosphere. The seasonality in the vapor flux convergence implied by Figure 3c is broadly in accord with the observed late summer/early autumn maximum in precipitation over the polar cap and Arctic Ocean [*Serreze et al.*, 2007]. For long-term annual averages, the vapor flux convergence equates to net precipitation (precipitation minus evaporation, or P − E). Several studies have examined P − E for the polar cap domain using NRA and ERA-15 vapor transports. Long-term annual means range from 182 to 207 mm [*Genthon*, 1998; *Cullather et al.*, 2000] compared to the ERA-40 value of 193 mm for the period 1979–2001.

[46] Recall that the net surface flux is the sum of the surface radiation and turbulent heat flux terms. As seen in Figure 3d, the vertical sensible and latent heat flux terms are small through the year. In winter, the small sensible heat flux tends to be directed toward the surface (i.e., negative, hence an atmospheric energy sink) in association with temperature inversion conditions. The small latent heat flux is, by contrast, always upward (an atmospheric heat source). The net longwave flux is considerably larger but, compared to the net shortwave flux, is rather steady through the year. The annual cycle of the net surface flux consequently mirrors the annual cycle in the surface net shortwave flux.

4.2. Spatial Patterns of the Net Surface Flux

[47] Maps of the net surface flux for the four midseason months from ERA-40 demonstrate the importance of the ocean (Figure 4). The salient features in January are intense upward fluxes over open ocean areas including the Norwegian and Greenland seas where there are very strong air-sea temperature gradients, smaller upward fluxes over the ice-covered ocean, and even smaller upward fluxes over land regions. For April, fluxes are still upward over ocean areas but of smaller magnitude and are downward over land. For July, fluxes are everywhere downward. They are largest over ocean areas south of the 80°N where strong ice melt can be expected and (further south) where low albedo open water areas promote strong solar heating, replenishing the oceanic sensible heat store. Note the sharp coastal contrasts in July. Warming of the atmosphere is strongly inhibited over the ocean compared to land. This sets up a summer Arctic frontal zone, providing favorable conditions for summer cyclogenesis, especially near the shores of eastern Eurasia and Alaska [*Serreze et al.*, 2001]. October depicts the transition back toward winter conditions, with large upward fluxes over open water areas and the coastal Arctic seas where thin ice is growing, compared to smaller fluxes over the central Arctic Ocean where sea ice is thicker. The study by *Trenberth and Stepaniak* [2004] provides a complementary analysis of seasonal changes in the net surface flux over ocean regions for 60°N to 60°S.

[48] The field of the annual mean net surface flux follows in Figure 5. Over the ocean, it is of the expected positive sign, with the largest values over the northern North Atlantic and Atlantic subpolar seas. As discussed with reference to Table 1, the values are likely too large. Assuming a steady state climate, the flux should be close to zero over land. However, according to ERA-40, the annual average flux over much of the land is between −5 and −10 W m^{-2} and locally greater. While these also seem much too large, the sign is likely correct as available observations point to subsurface warming. Recent positive trends in surface air temperature over Arctic lands encompass all seasons [*Serreze and Francis*, 2006], and warming of near surface permafrost has been documented for Alaska, especially on the North Slope [*Osterkamp*, 2005], Canada [*Smith et al.*, 2005], and Russia [*Pavlov and Moskalenko*, 2002]. An increase in active layer thickness over permafrost (the maximum depth of seasonal thaw) could be allied with a prominent downward flux as it involves phase change in the surface layer which is often ice rich. At least for Russia, there is strong evidence for increasing active layer depth [*Zhang et al.*, 2005].

4.3. Zonal Asymmetry of Atmospheric Energy Flow

[49] Figure 6 shows longitudinal variations by month of the vertically integrated meridional flow of total atmospheric energy and the latent heat component across 70°N in units of gigawatts per meter (GW m^{-1} = 10^9 W m^{-1}) based on ERA-40. Results from NRA are, in general, very similar and are not shown.

[50] Looking first at total energy (Figure 6a), there is a prominent region of poleward (positive) flow centered at about 50°W. This is just east of the axis of the mean 500-hPa eastern North American trough, pointing to contributions from the time mean flow and eddy transports associated with the North Atlantic storm track. These are strongest in winter and weakest in summer. A strong region of equatorward (negative) flow lies to the west, centered at about 110°W, associated with the descending leg of the 500-hPa western North American ridge. These are again strongest in winter. Over Eurasia, centered at about 150°E, is a region of inflow during the cold season and weak

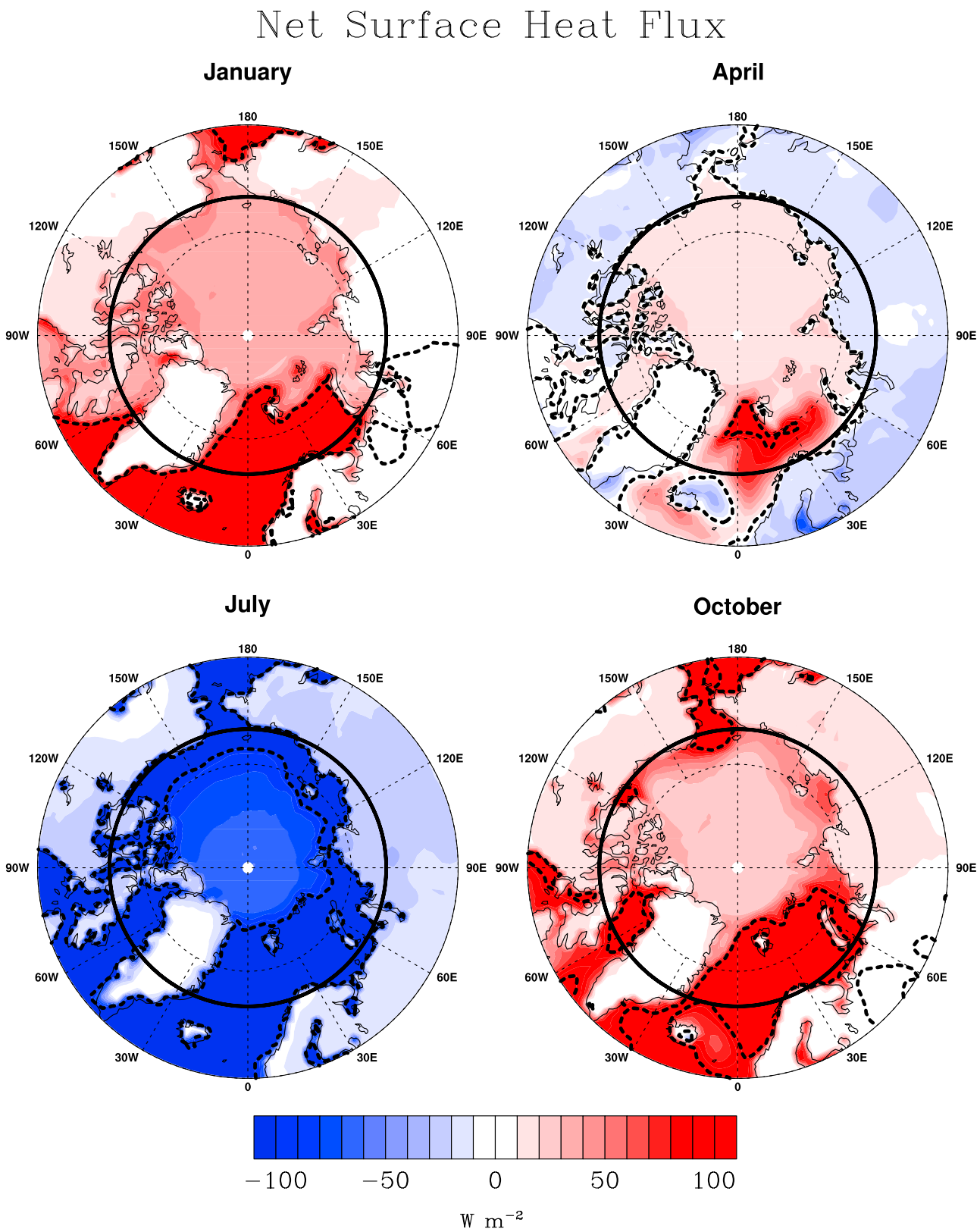

Figure 4. Maps of the net surface heat flux from ERA-40 for January, April, July, and October extending down to 60°N. The 70°N latitude circle is indicated in bold. The −100, 0, and 100 W m^{-2} contours are shown as dashed lines. Areas in white are ±10 W m^{-2}.

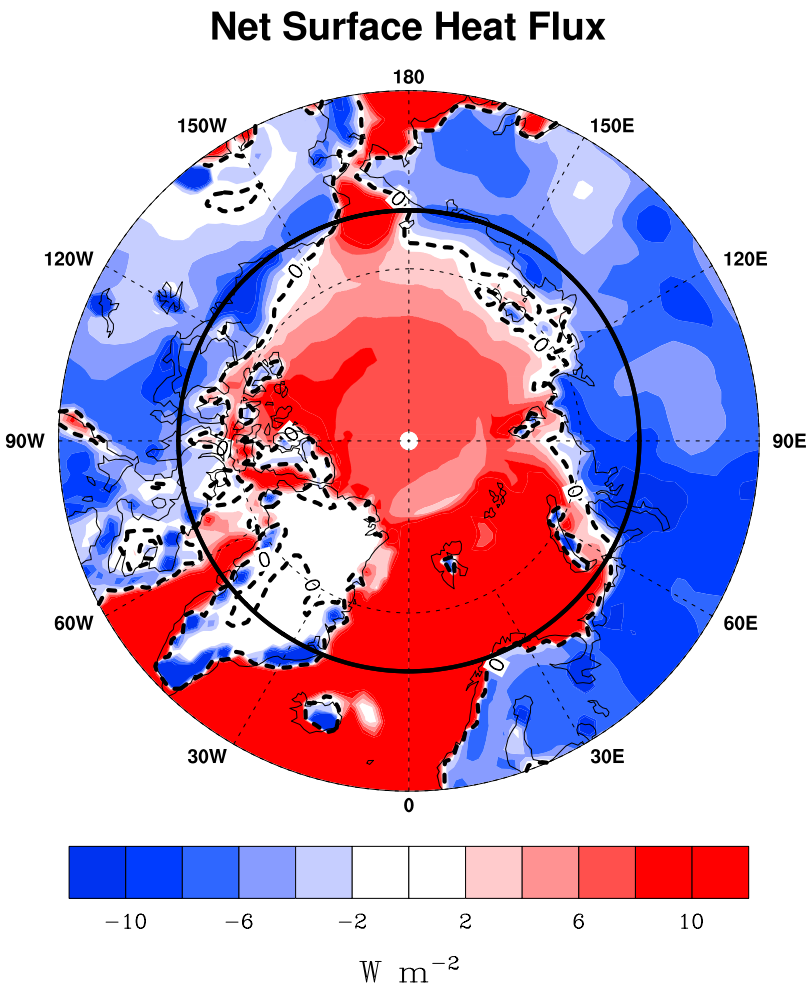

Figure 5. Map of the annual mean net surface heat flux from ERA-40 extending down to 60°N. The 70°N latitude circle is indicated in bold. The 0 W m^{-2} contour is shown as dashed lines. Areas in white are ±2 W m^{-2}.

outflow in summer. In winter, this longitude is just downstream of the East Asian trough. The trough weakens and shifts east in summer, helping to account for the outflows in this season. Finally, outflow dominates a broad region from about 30°E to 90°E, with the longitude of the maximum varying by season. This shows a broad correspondence with mean equatorward winds on the western limb of the Urals trough.

[51] The only notable difference between ERA-40 latent heat transport (Figure 6b) and that of NCEP is that the peaks are somewhat stronger in ERA-40, perhaps because of this model's higher resolution. Recall from Figure 3c that the zonally averaged meridional latent heat transport exhibits a summer/early autumn peak. It is evident that this is largely the result of strong moisture inflows in four regions. These more than compensate for the strong outflows centered at about 110°W. The area of inflow at around 90°E is slightly east of the Urals trough (during summer, the trough axis at 500 hPa is at about 80°E). In turn, the area of summer inflow at about 165°W is just east of the East Asian trough. Prominent inflows at about 50°W and near the prime meridian are separated by a region of equatorward flow in summer and weak poleward flow in the other seasons. This separation manifests blocking by the Greenland ice sheet. Most of the moisture flow occurs below 700 hPa (roughly 3000 m). At 70°N, the highest ice sheet elevations of about 2900 m are found at about 35°W longitude.

4.4. Time Series of Atmospheric Transport and Storage

[52] Monthly time series of the energy transport and its components from ERA-40 and NRA are plotted in Figure 7. The ERA-40 results extend from 1979 to 2001. Those for NRA are for the longer record 1979–2005. Units are in petawatts (PW = 10^{15} W). Division by the area of the polar cap would yield W m^{-2}.

[53] The two reanalyses are remarkably close in the transports of sensible heat. They are also close in their depiction of the kinetic energy and latent heat transports, but with a tendency for NRA to yield slightly larger peak summer values in the latter as well as slightly larger winter values. Compared even to the latent heat transport, the kinetic energy term is quite small. There is less agreement in the geopotential transport, particularly in the early part of the record, when ERA-40 is lower than NRA. We calculated the ERA-40 geopotential transports both from the archived fields of this term and by subtracting the sensible, kinetic,

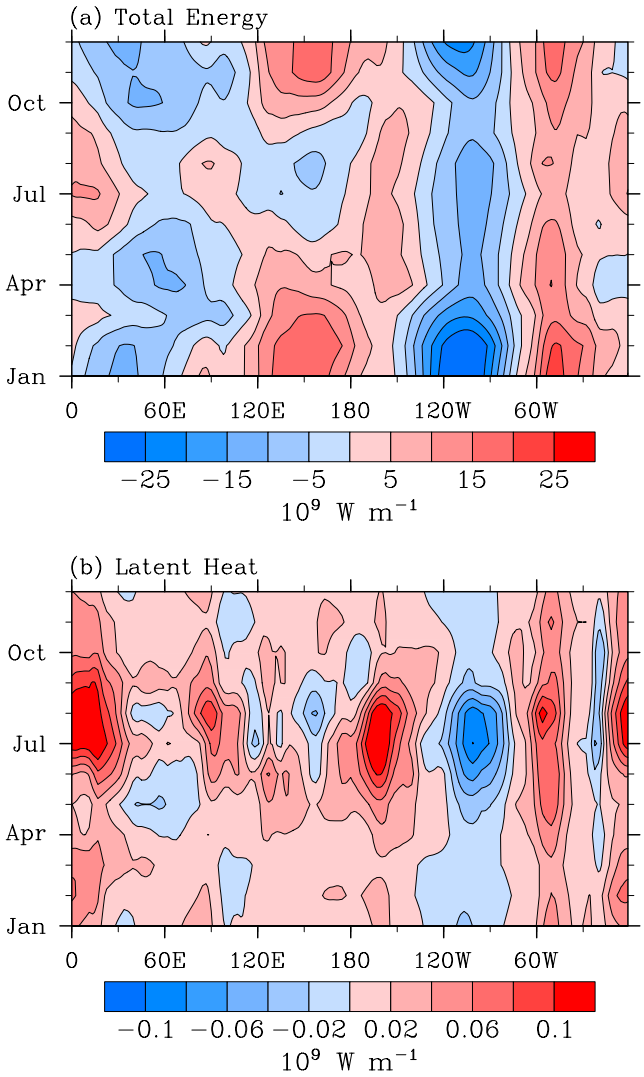

Figure 6. Annual cycle of the vertically integrated flow of: (a) total atmospheric energy; (b) latent heat from ERA-40 across 70°N by longitude.

and latent heat transports from the total transports. The time series do not match, but should. The cause of this discrepancy is not clear. The geopotential transport shown in Figure 7 is based on the latter (residual) calculation, which compares better with NRA. Assuming that this is the correct representation of the ERA-40 transport, the remaining departures from NRA may involve several issues, such as assimilation of satellite data and the higher vertical resolution of ERA-40 in the upper troposphere and stratosphere. Since geopotential is very large at high atmospheric levels, and noting that the geopotential transport tends to peak in the upper troposphere, even small percentage differences in geopotential between the two reanalysis could yield a significant difference. There are also potential issues with NRA. *Trenberth and Stepaniak* [2002] documented a "pathological problem" with NRA in the stratosphere, most pronounced where topographic gradients are steep and the magnitude of the wind increases with height in the stratosphere. This appears to be related to use of the terrain-following (sigma) coordinate system and the upper boundary condition in the assimilating model.

[54] Departures between the two reanalyses in total energy transport hence primarily result from departures in the geopotential and latent heat terms. In particular, compared to NRA, ERA-40 depicts smaller total transports for about the first 5 years of the record. In the later part of the common period of record, there is more agreement.

[55] Figure 8 compares monthly time series of the stores of sensible heat and latent heat. The annual cycle is of course very prominent. Sensible heat storage always tends to be somewhat higher in ERA-40. While reasons for this are not clear, it may contribute to problems in the TOA radiation budget in ERA-40 discussed earlier. Warm biases relative to NRA are readily evident in ERA-40 surface air temperatures over the Arctic (I. Rigor, personal communication, 2006).

[56] The Arctic is known to be in the midst of pronounced change, characterized by increases in surface air temperature (SAT) in recent decades [*Serreze and Francis*, 2006] and strong reductions in sea ice extent, especially in September (http://www.nsidc.org [*Stroeve et al.*, 2005]). As discussed earlier, there are indications of subsurface warming over land and rising active layer thickness over permafrost. Other studies demonstrate increases in oceanic heat transport into the Arctic Ocean through Bering Strait and Fram Strait [*Woodgate et al.*, 2006; *Schauer et al.*, 2004].

[57] *Graversen* [2006] argued that rises in Arctic SAT as depicted in ERA-40 over the period 1979–2001 can be partly explained by a weak positive trend in poleward atmospheric energy transport. Our investigations of the longer NRA record point to pronounced surface and lower troposphere warming in recent years (2000–2005), as well as a small but significant positive trend in annual mean latent heat storage (1979–2005). However, at least for the polar cap, there is little evidence from either reanalysis for increases in vertically integrated sensible heat storage. These findings must acknowledge that trend assessments from reanalysis are fraught with uncertainty (see the study by *Trenberth et al.* [2005] regarding trends in column water vapor and the work of *Trenberth and Smith* [2006] for spurious temperature trends in ERA-40).

5. Energy Budget of the Arctic Ocean Domain

5.1. Details of the Calculations

[58] Attention now turns to linking the atmospheric and oceanic budgets for the Arctic Ocean domain (Figure 1). ERA-40 provides all terms of the atmospheric budget. From equation (5), the change in heat storage of the ocean ($\partial O_E/\partial t$) is expressed as the sum of the vertical net surface flux F_{sfc}, the divergence of latent heat in the form of snow and ice $\nabla \bullet \mathbf{F}_i$, and the oceanic convergence of sensible heat $-\nabla \bullet \mathbf{F}_o$. The change in ocean heat storage is partitioned into changes in sensible heat storage in snow and ice (S_i), sensible heat storage in the water (S_o), and latent heat storage in snow and ice (L_i). As justified from calculations with suitably assumed temperatures, S_i can be ignored. With this assumption, and having monthly estimates of all major terms except L_i, the unknown L_i is obtained as a residual.

[59] Recall that estimates of $\nabla \bullet \mathbf{F}_i$ are based on the Fram Strait ice export using data from the study by *Vinje et al.* [1998]. For $-\nabla \bullet \mathbf{F}_o$, reliance is placed on output from a

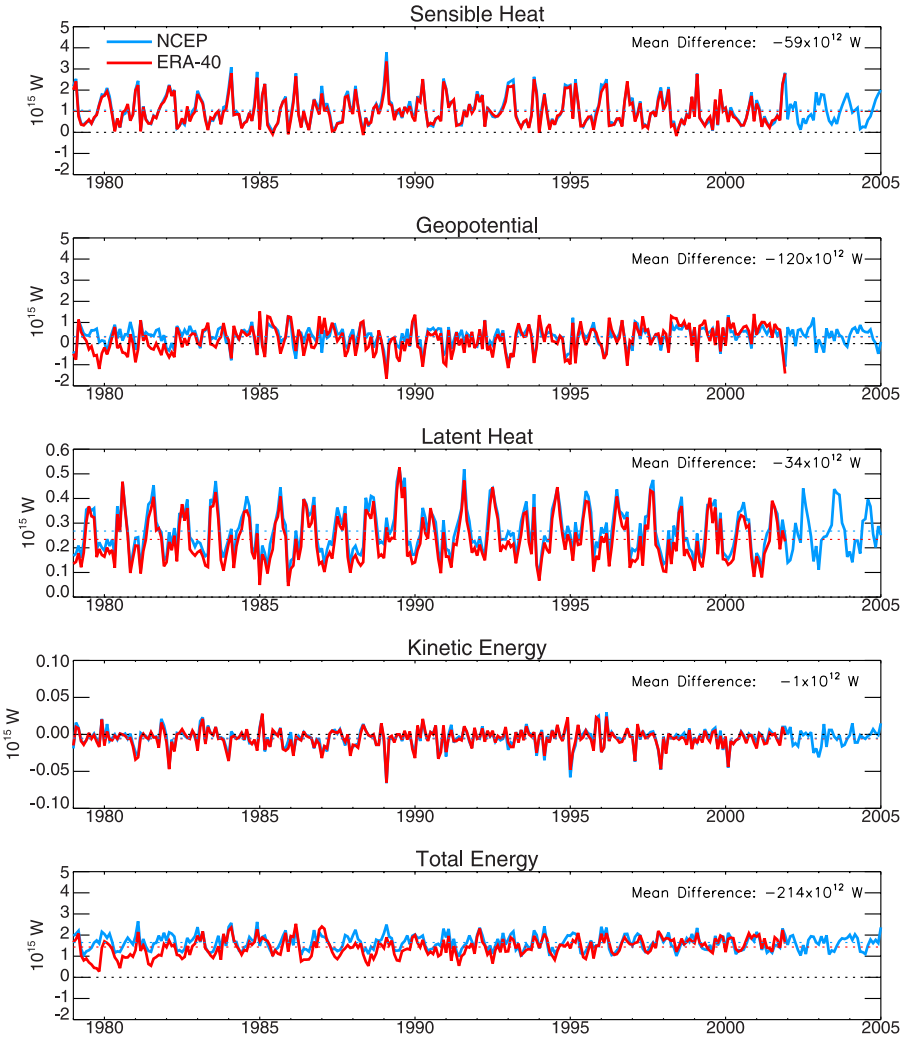

Figure 7. Monthly time series of the components of atmospheric transport from ERA-40 (1979–2001) and NRA (1979–2005) across 70°N. Mean differences (ERA-40 minus NRA) are shown for each component and at 3 orders-of-magnitude less than the *y* axis scales.

run of PIOM (see section 3.4 [*Zhang*, 2005]). The oceanic sensible heat convergence represents the sum of transports through Fram Strait, the Barents Sea opening, Bering Strait, and the Canadian Arctic Archipelago. Following common convention [e.g., *Maslowski et al.*, 2004], transports are computed with respect to a reference temperature of −0.10°C. Unfortunately, subannual information on modeled heat fluxes was only archived as seasonal means (JFM = winter, AMJ = spring, JAS = summer, OND = autumn). For the annual cycle, the seasonal means were repeated for each month within a season.

[60] Changes in oceanic sensible heat storage are calculated from the PHC data set (section 3.4). The depth to which the annual cycle of temperature penetrates was first determined. This is about 500 m in the Nordic Seas, 250 m in the Barents Sea, and about 100 m in the central Arctic Ocean. We then found the mean potential temperature of the ocean from 500 m to the bottom. This value (−0.27°C) was taken to be the reference temperature. Monthly sensible heat storage was then calculated with respect to this reference. These estimates represent the heat content of an annually varying upper 0 to 500 m layer relative to the deep 500 m bottom layer that does not vary intra-annually. As the PHC records are only sufficient to obtain climatological means, the monthly tendencies were obtained from center differencing (for example, the June tendency is the heat content in W m^{-2} for July minus May, divided by 2). We estimate about a 2% error in the monthly sensible heat content values. The largest source of error is interpolation error, which is much larger than the instrument error.

5.2. Results

[61] Results are summarized in Table 2. Looking first at annual mean conditions, it is apparent that there is a substantial residual in the atmospheric budget. For the polar cap domain, the residual is small in an annual sense (−1 W m^{-2}). However, for the smaller Arctic Ocean domain, it is a full −20 W m^{-2}. For individual months, residuals are negative except for June and reach −35 W m^{-2} in January and February.

[62] Assuming steady state, the tendency in annual oceanic heat storage, like that for atmospheric heat storage shown in

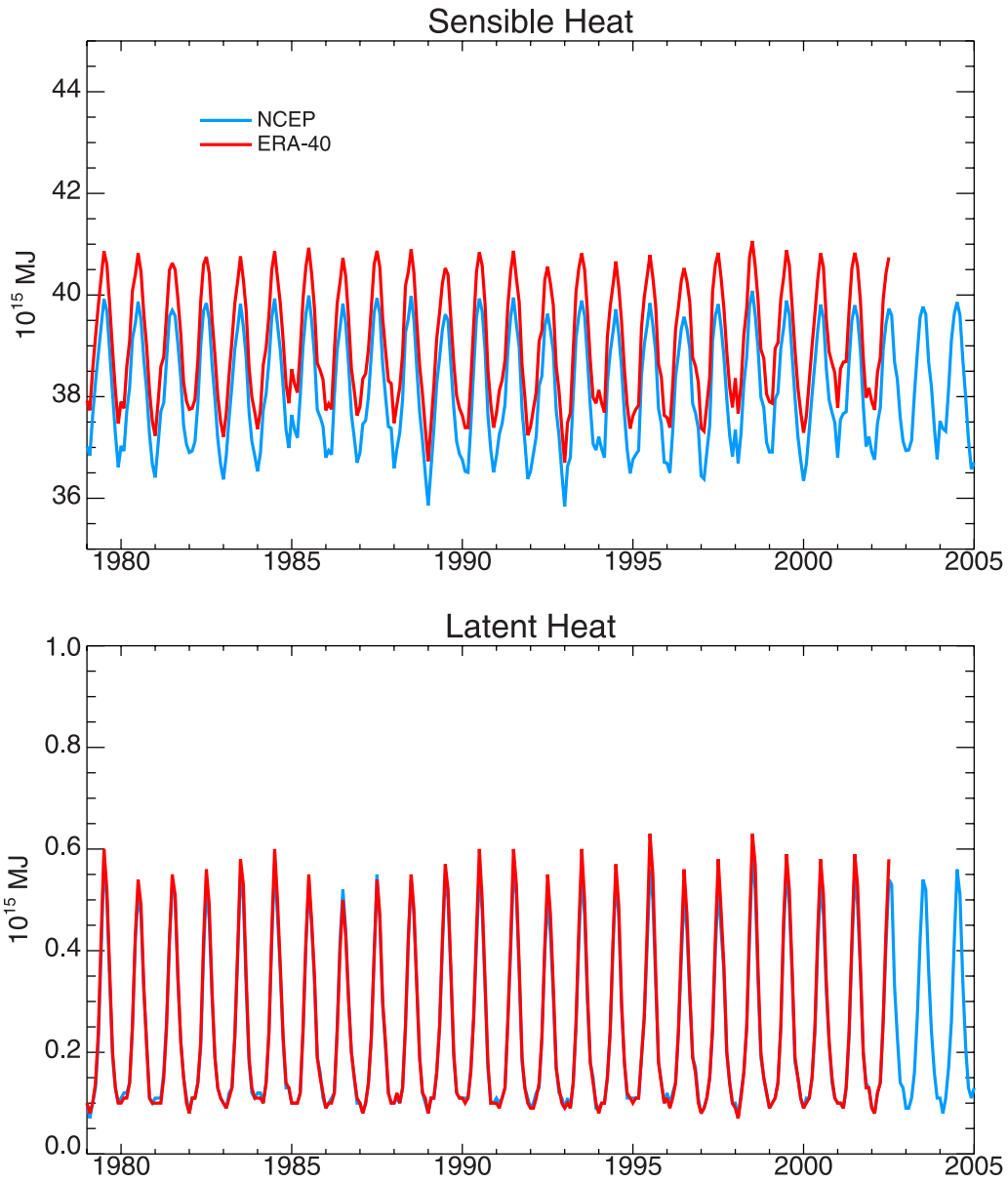

Figure 8. Monthly time series of sensible and latent heat storage for the polar cap from ERA-40 (1979–2001) and NRA (1979–2005).

Table 2, should be approximately zero. However, our calculations yield a mean annual loss of oceanic heat of 5 W m^{-2}. The conclusion must be that either the net surface flux from ERA-40 of 11 W m^{-2} is too large or that the sum of $-\nabla \bullet \mathbf{F}_o$ and $\nabla \bullet \mathbf{F}_i$ is too small. As argued below, the former can be implicated. Calculating F_{sfc} as a residual from the atmospheric transport and the TOA net radiation yields an absurd value of 31 W m^{-2}. This again argues that the annual mean energy budget residual is strongly tied to problems in the ERA-40 TOA radiation budget.

[63] The ice transport term seems fairly well constrained. The value of 3 W m^{-2} calculated from *Vinje et al.* [1998] estimate of the Fram Strait ice volume transport data is about 20% higher than obtained from the estimates of *Kwok et al.* [2004]. While this difference is large in terms of freshwater transport [*Serreze et al.*, 2007], in terms of energy associated with the latent heat transport, it is less than 1 W m^{-2}. The estimate of *Kwok et al.* [2004] is based on ULS observations of ice thickness and velocities obtained from a feature-tracking algorithm applied to satellite passive microwave data.

[64] The annual mean oceanic heat convergence of 3 W m^{-2} from PIOM used in Table 2 is largely driven by the inflow of relatively warm waters of Atlantic origin through Fram Strait and the Barents Sea opening. *Simonsen and Haugen* [1996] summarized oceanic heat transports through the major straits from the observationally based studies of *Rudels* [1987] and *Hopkins* [1991]. Taking the sum of these transports and averaging over the Arctic Ocean domain reveals that the PIOM estimate is close to that of *Rudels* [1987] but roughly half that of *Hopkins* [1991]. If the latter is used as an upper limit (6 W m^{-2}), the implied net surface heat flux would be about 9 W m^{-2}. These comparisons, however, must be tempered by recognition

Table 2. Monthly and Annual Mean Energy Budget Terms for the Arctic Ocean Domain

	Fluxes and Storage Changes									
Month	$\partial A_E/\partial t$	R_{top}	$-\nabla \bullet \mathbf{F}_A$	F_{sfc}	$\partial O_E/\partial t$	S_o	L_i[a]	$\nabla \bullet \mathbf{F}_i$	$-\nabla \bullet \mathbf{F}_o$	Res.[b]
January	−4	−178	81	58	−52	−19	−33	3	3	−35
February	4	−175	91	53	−47	−16	−31	3	3	−35
March	12	−150	93	41	−34	−9	−25	4	3	−28
April	25	−96	72	20	−14	6	−20	4	2	−29
May	20	−37	44	−14	18	27	−9	3	2	−27
June	19	16	79	−75	79	40	40	3	2	1
July	2	10	91	−100	105	35	69	2	3	−1
August	−17	−68	92	−45	50	11	39	1	3	−4
September	−28	−150	95	18	−13	−5	−8	2	3	−9
October	−22	−186	97	58	−52	−4	−48	3	3	−9
November	−11	−186	85	59	−53	−29	−25	3	3	−31
December	2	−180	90	59	−52	−37	−15	4	3	−33
Mean	0	−115	84	11	−5	0	−5	3	3	−20

[a] L_i is calculated as the difference between the measured terms $\partial O_E/\partial t$ and S_o.
[b] The residual is calculated as $R_{top} - \nabla \bullet \boldsymbol{F}_A + F_{sfc} = \partial O_E/\partial t$.

that the Barents Sea opening used in the summary of *Simonsen and Haugen* [1996] extends from Svalbard to the eastern end of Novaya Zemlya which is different than used in the present study. As for other estimates, *Schauer et al.* [2004] reported transports through Fram Strait ranging from 1.7 to 4.3 W m^{-2} when averaged over the Arctic Ocean domain. For the combined Fram Strait and Barents Sea openings, the modeling study of Maslowski yields a value of 2.5 W m^{-2}.

[65] Putting these estimates together, the ocean heat flux convergence of 3 W m^{-2} from PIOM seems reasonable, as does the ice outflow term of 3 W m^{-2}. This implies that the annual mean net surface flux for the Arctic Ocean domain should be about 6 W m^{-2}.

[66] Looking at the annual cycles, the Arctic Ocean and polar cap show the same qualitative seasonality in the atmospheric terms. Interestingly, the July atmospheric transport is larger than for January. While consistent with the very large net surface flux in July, which strongly draws heat out of the atmosphere and (from a budget requirement) requires a strong atmospheric transport, this argument must acknowledge the large energy budget residuals. As the horizontal ocean flux terms are fairly small and steady, the annual cycle in total ocean heat storage is essentially determined by the net surface flux.

[67] From the PHC data, the summer gain in oceanic sensible heat is largest in June and July, and the largest heat losses occur in November and December. Ice melt (positive L_i) occurs from June through August, largest in July when it is about twice as big as the sensible heat gain. The latter will occur mostly in open water areas. The strongest ice growth (negative L_i) is indicated for October, followed by a decline between November and December, and then another peak in January and February. The autumn peak is expected: There is ample open water in which new ice can grow. The second peak is puzzling. Intuitively, one might expect the October peak to be followed by declining ice growth through winter (as ice thickens, the temperature gradient between the surface and ice/ocean interface declines) or somewhat steady growth. The latter recognizes that air temperatures also decline to a January minimum and that production of new, thin ice will continue in the "ice factory" along the Siberian coast where offshore ice motion produces numerous leads (openings in the cover) where new ice can form.

[68] These results can be partly explained by delayed ice growth in the warmer parts of the Arctic Ocean domain, specifically in the Barents Sea region. The annual cycle in oceanic sensible heat storage from the PHC (Figure 9) turns out to be dominated by the Barents Sea, which, compared to other regions, is fairly well sampled throughout the year from hydrographic surveys. Seasonal changes in sensible heat storage over the rest of the Arctic Ocean are much smaller. Looking back at Figure 4, the Barents Sea region is characterized by strong autumn and winter cooling and strong summer heating of the upper ocean via the net surface flux. However, autumn cooling of the column in this region is delayed because of oceanic heat advection through the Barents Sea opening (the Barents Sea Branch of the Atlantic inflow). This is evident in the Barents Sea analysis of *Fuverik* [2001]. Near the surface (10 m), peak water temperatures occur in mid-August, then fall sharply into December, attaining minimum values in mid-March. However, at progressively deeper depths, the seasonal temperature maximum occurs progressively later, from mid-September at 50 m to mid-October at 300 m (albeit quite

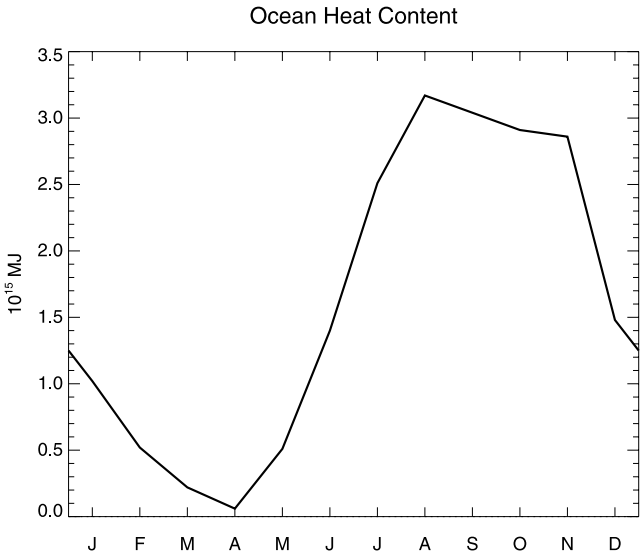

Figure 9. Annual cycle of oceanic sensible heat content from the PHC data set.

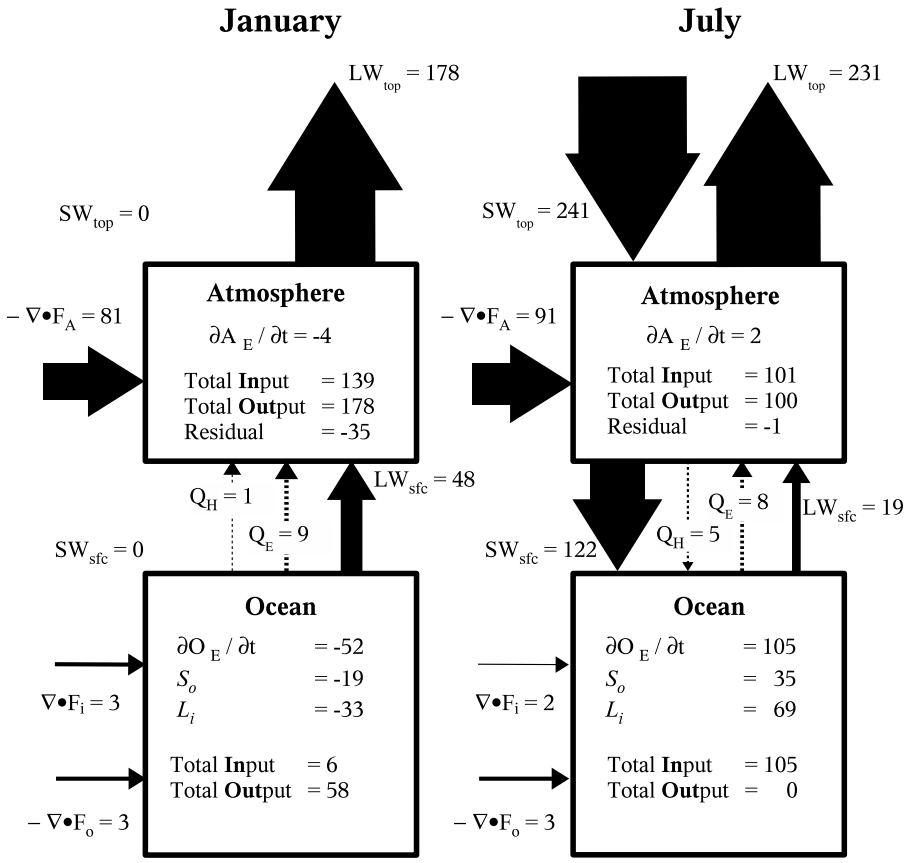

Figure 10. Schematic of the energy budgets of the Arctic Ocean domain for: (a) January and (b) July, based on the information in Table 2. The width of the arrows is proportional to the size of the transports. Atmospheric and surface terms are defined as in Figure 3.

subdued). In other words, even as the surface waters cool, the ocean circulation keeps bringing heat into the region. This compensation helps to explain the rather high November sensible heat content. The water column then cools strongly between November and December. However, there is still enough heat storage to prevent much ice growth until January and February.

[69] Errors in the calculated tendencies may play a contributing role. Because of the relatively high sensible heat content in November and the much lower value in January (Figure 9), the December tendency based on a centered difference (January minus November divided by 2) is likely too large (Table 2). Were sufficient daily data available to calculate tendencies in the same way as done with the atmospheric storages, a smaller tendency would be obtained, leading to a larger ice growth in this month. Shortcomings of center differencing will also influence tendencies in other months. Errors in the ERA-40 net surface flux must also be considered. As changes in total oceanic heat content are primarily determined by the net surface flux, errors in this term will directly impact on the partitioning between ice growth/melt and sensible heat gain/loss.

[70] To summarize the sharp seasonality in the atmospheric and oceanic budgets, Figure 10 shows results in schematic form for January and July, but with more complete breakdown of the top of atmosphere and surface terms. The width of each arrow is proportional to the size of the transport. The dominant contrasts are the strong net radiation loss to space in January compared to a small net radiative gain in July, attended by a large upward net surface flux (January) that removes heat from the ocean and a strong downward net surface flux (July) that warms the ocean, respectively, largely associated with the net shortwave flux. Reiterating shortcomings in ERA-40, there is a very large residual in the atmospheric budget for January of -35 W m^{-2}. As the ice growth/melt term is calculated as a residual, the ocean budgets are of course closed. As part of a follow-on study, CERES and ERBE data could be used to adjust the ERA-40 TOA radiation fluxes, with these revised values then used to reevaluate the net surface flux.

6. Conclusions

[71] Building on the work of *Nakamura and Oort* [1988], this study indicates that the net surface flux has first-order impacts on the atmospheric energy budgets of both the polar cap and Arctic Ocean domain. Because horizontal oceanic heat flux convergence and sea ice transport out of the Arctic via Fram Strait are fairly small, the net surface flux is in turn the primary driver of seasonal changes in ocean heat storage. From autumn into winter, the atmosphere cools in response to the declining solar flux. However, the net surface flux turns positive largely because of sea ice growth and sensible heat loss from the ocean. These processes add significant heat to the atmosphere, which can be viewed as reducing the requirements for transports via the atmosphere.

The solar flux grows from spring into summer and the atmosphere gains energy. However, the net surface flux turns strongly negative. This is primarily related to sea ice melt and replenishment of the ocean's reservoir of sensible heat. For the Arctic Ocean domain, the July net surface flux from ERA-40 is larger than the atmospheric transport.

[72] An interesting point is that while the export of sea ice through Fram Strait is a minor component of the ocean heat budget, it is a very large term in the Arctic Ocean's freshwater budget, representing 25% of the total freshwater export on an annual mean basis. Similarly, while the import of oceanic heat through Bering Strait is also a small component of the oceanic heat budget, this current accounts for about 30% of the total freshwater input to the Arctic Ocean [*Serreze et al.*, 2007].

[73] While ERA-40 provides for a valuable description of the basic atmospheric energy budget, it also has shortcomings. There are substantial residuals in the budget. While in large part these likely stem from deficiencies in top-of-atmosphere radiation, a suite of other issues are presumably involved, including aspects of the net surface flux (which appear to be too large in the annual mean) and remaining mass balance errors in the atmospheric transports. With regard to the transports and energy storages, there are also a number of differences with respect to NRA. Efforts to define the energy budget of the ocean are also met with difficulty, notably uncertainties in monthly changes in its sensible heat content and partitioning changes in total ocean heat storage between sensible and latent heat.

[74] **Acknowledgments.** This study was supported by NASA contracts NNG06GB26G, NNG04GH52G, NNG04GB03G, NSF grants OPP-0229651, ARC-0531040, and ARC-0531103, and NOAA. W. Ermold is thanked for programming assistance. The National Center for Atmospheric Research is sponsored by the National Science Foundation.

References

Allan, R. P., M. A. Ringer, J. A. Pamment, and A. Slingo (2004), Simulation of the Earth's radiation budget by the European Centre for Medium-Range Weather Forecasts 40-year reanalysis (ERA40), *J. Geophys. Res.*, *109*, D18107, doi:10.1029/2004JD004816.

American Meteorological Society (2000), *Glossary of Meteorology*, 2nd edition, 855 pp., Am. Meteorol. Soc., Boston, Mass.

Antonov, J. I., S. Levitus, T. P. Boyer, M. E. Conkright, T. D. O'Brien, and C. Stephens (1998), *World Ocean Atlas 1998 Vol. 1: Temperature of the Atlantic Ocean*, NOAA Atlas NESDIS 27, 166 pp.

Beesley, J. A., and R. E. Moritz (1999), Toward an explanation of the annual cycle of cloudiness over the Arctic Ocean, *J. Clim.*, *12*, 395–415.

Boyer, T. P., S. Levitus, J. I. Antonov, M. E. Conkright, T. D. O'Brien, and C. Stephens (1998), *World Ocean Atlas 1998 Vol. 4: Salinity of the Atlantic Ocean*, NOAA Atlas NESDIS 30, 166 pp.

Bromwich, D. H., S.-H. Wang, and A. J. Monaghan (2002), ERA-40 representation of the Arctic atmospheric moisture budget, *ERA-40 Project Report Series 3. Workshop on Re-Analysis, 5–9 November, 2001*, European Center for Medium Range Weather Forecasts, pp. 287–297.

Cullather, R. I., D. H. Bromwich, and M. C. Serreze (2000), The atmospheric hydrologic cycle over the Arctic basin from reanalyses, Part I: Comparisons with observations and previous studies, *J. Clim.*, *13*, 923–937.

Environmental Working Group (EWG) (1997), *Joint U.S.-Russian Atlas of the Arctic Ocean for the Winter Period*, National Snow and Ice Data Center, CD-ROM.

Environmental Working Group (EWG) (1998), *Joint U.S.-Russian Atlas of the Arctic Ocean for the Summer Period,* National Snow and Ice Data Center, CD-ROM.

Fuverik, T. (2001), Annual and interannual variability of Atlantic water temperatures in the Norwegian and Barents Seas: 1980–1996, *Deep Sea Res. Part I*, *48*, 383–404.

Genthon, C. (1998), Energy and moisture flux across 70°N and S from ECMWF Re-Analysis, Proc. First WCRP Int. Conf. on Reanalyses, WCRP-104 9WMO/TD-No. 876), Silver Spring, MD, WMO, pp. 371–374.

Graversen, R. G. (2006), Do changes in the midlatitude circulation have any impact on the Arctic surface air temperature trend?, *J. Clim.*, *19*, 5422–5438.

Herman, G., and R. Goody (1976), Formation and persistence of summertime Arctic stratus clouds, *J. Atmos. Sci.*, *33*, 1537–1553.

Hopkins, T. S. (1991), The GIN Sea—A synthesis of its physical oceanography and literature review 1972–1985, *Earth Sci. Rev.*, *30*, 175–319.

Kalnay, E., et al. (1996), The NCEP/NCAR 40-year reanalysis project, *Bull. Am. Meteorol. Soc.*, *77*, 437–471.

Kato, S., N. G. Loeb, P. Minnis, J. A. Francis, T. P. Charlock, D. A. Rutan, E. E. Clothiaux, and S. Sun-Mack (2006), Seasonal and interannual variations of top-of-atmosphere irradiance and cloud cover over polar regions derived from the CERES data set, *Geophys. Res. Lett.*, *33*, L19804, doi:10.1029/2006GL026685.

Key, J. R., and J. Intrieri (2000), Cloud particle phase determination with AVHRR, *J. Appl. Meteorol.*, *36*, 1797–1805.

Key, J. R., X. Wang, J. Stroeve, and C. Fowler (2001), Estimating the cloudy sky albedo of sea ice and snow from space, *J. Geophys. Res.*, *106*, 12,489–12,497.

Kistler, R., et al. (2001), The NCEP-NCAR 50-year reanalysis: Monthly means CD-ROM and documentation, *Bull. Am. Meteorol. Soc.*, *82*, 247–267.

Kwok, R., G. F. Cunningham, and S. S. Pang (2004), Fram Strait ice outflow, *J. Geophys. Res.*, *109*, C01009, doi:10.1029/2003JC001785.

Kwok, R., W. Maslowski, and S. W. Laxon (2005), On large outflows of Arctic sea ice into the Barents Sea, *Geophys. Res. Lett.*, *32*, L22503, doi:10.1029/2005GL024485.

Maslowski, W., D. Marble, W. Walczowski, U. Schauer, J. L. Clement, and A. J. Semptner (2004), On climatological mass, heat, and salt transports through the Barents Sea and Fram Strait from a pan-Arctic coupled ice-ocean model simulation, *J. Geophys. Res.*, *109*, C03032, doi:10.1029/2001JC001039.

Nakamura, N., and A. H. Oort (1988), Atmospheric heat budgets of the polar regions, *J. Geophys. Res.*, *93*(D8), 9510–9524.

Osterkamp, T. E. (2005), The recent warming of permafrost in Alaska, *Global Planet. Change*, *49*, 187–202, doi:10.1016/j.gloplacha.2005.09.001.

Overland, J. E., and P. Turet (1994), Variability of the atmospheric energy flux across 70°N computed from the GFDL data set, In: The Polar Oceans and their Role in Shaping the Global Environment, The Nansen Centennial Volume, edited by R. D. Muench and J. E. Overland, *Geophys. Monogr.*, *85*, pp. 313–325, AGU, Washington, D. C.

Pavlov, A. V., and N. G. Moskalenko (2002), The thermal regime of soils in the north of western Siberia, *Permafr. Periglac. Process.*, *13*, 43–51.

Rogers, A. N., D. H. Bromwich, E. N. Sinclair, and R. I. Cullather (2001), The atmospheric hydrologic cycle over the Arctic basin from reanalyses, Part II: Interannual variability, *J. Clim.*, *14*, 2414–2429.

Rudels, B. (1987), On the mass balance of the Polar Ocean with special emphasis on the Fram Strait, *Skr. Nor. Polarinst.*, *188*, 1–53.

Schauer, U., E. Fahrbach, S. Osterhus, and G. Rohardt (2004), Arctic warming through the Fram Strait: Oceanic heat transport from 3 years of measurements, *J. Geophys. Res.*, *109*, C06026, doi:10.1029/2003JC001823.

Semmler, T., D. Jacob, K. H. Schlunzen, and R. Podzun (2005), The water and energy budget of the Arctic atmosphere, *J. Clim.*, *18*, 2515–2530.

Serreze, M. C., and J. A. Francis (2006), The Arctic amplification debate, *Clim. Change*, *76*, doi:10.10007/s10584-005-9017-y.

Serreze, M. C., and C. M. Hurst (2000), Representation of mean Arctic precipitation from NCEP-NCAR and ERA reanalyses, *J. Clim.*, *13*, 182–201.

Serreze, M. C., J. R. Key, J. E. Box, J. A. Maslanik, and K. Steffen (1998), A new monthly climatology of global radiation for the Arctic and comparisons with NCEP-NCAR reanalysis and ISCCP-C2 fields, *J. Clim.*, *11*, 121–136.

Serreze, M. C., A. H. Lynch, and M. P. Clark (2001), The Arctic frontal zone as seen in the NCEP/NCAR reanalysis, *J. Clim.*, *14*, 1550–1567.

Serreze, M. C., D. H. Bromwich, M. P. Clark, A. J. Etringer, T. Zhang, and R. Lammers (2003), The large-scale hydroclimatology of the terrestrial Arctic drainage, *J. Geophys. Res.*, *108*(D2), 8160, doi:10.1029/2001JD000919.

Serreze, M. C., A. Barrett, and F. Lo (2005), Northern high latitude precipitation as depicted by atmospheric reanalysis and satellite retrievals, *Mon. Weather Rev.*, *133*, 3408–3430.

Serreze, M. C., A. P. Barrett, A. G. Slater, R. A. Woodgate, K. Aagaard, R. Lammers, M. Steele, R. Moritz, M. Meredith, and C. M. Lee (2007), The large-scale freshwater cycle of the Arctic, *J. Geophys. Res.*, *111*, C11010, doi:10.1029/2005JC003424.

Simonsen, K., and P. M. Haugen (1996), Heat budgets of the Arctic Mediterranean and sea surface heat flux parameterizations for the Nordic Seas, *J. Geophys. Res.*, *101*(C3), 6533–6576.

Smith, S. L., M. M. Burgess, D. Riseborough, and F. M. Nixon (2005), Recent trends from Canadian permafrost thermal monitoring network sites, *Permafr. Periglac. Process.*, *16*, 19–30.

Steele, M., R. Morley, and W. Ermold (2001), PHC: A global ocean hydrography with a high-quality Arctic Ocean, *J. Clim.*, *14*, 2079–2087.

Stroeve, J., M. C. Serreze, F. Fetterer, T. Arbetter, W. Meier, J. Maslanik, and K. Knowles (2005), Tracking the Arctic's shrinking ice cover: Another extreme September minimum in 2004, *Geophys. Res. Lett.*, *32*, L04501, doi:10.1029/2004GL021810.

Su, F., J. C. Adam, K. E. Trenberth, and D. P. Lettenmaier (2006), Evaluation of surface water fluxes of the pan-Arctic land region with a land surface model and ERA-40 reanalysis, *J. Geophys. Res.*, *111*, D05110, doi:10.1029/2005JD006387.

Trenberth, K. E. (1997), Using atmospheric budgets as a constraint on surface fluxes, *J. Clim.*, *10*, 2796–2809.

Trenberth, K. E., and J. M. Caron (2001), Estimates of meridional atmosphere and ocean heat transports, *J. Clim.*, *15*, 3443–4344.

Trenberth, K. E., and L. Smith (2006), The vertical structure of temperature in the tropics: Different flavors of El Nino, *J. Clim.*, *19*, 4956–4973.

Trenberth, K. E., and A. Solomon (1993), Implications of global atmospheric spatial spectra for processing and displaying data, *J. Clim.*, *6*, 531–545.

Trenberth, K. E., and A. Solomon (1994), The global heat balance: Heat transports in the atmosphere and ocean, *Clim. Dyn.*, *10*, 107–134.

Trenberth, K. E., and D. P. Stepaniak (2002), A pathological problem with NCEP reanalyses in the stratosphere, *J. Clim.*, *15*, 690–695.

Trenberth, K. E., and D. P. Stepaniak (2003), Co-variability of components of poleward atmospheric energy transports on seasonal and interannual timescales, *J. Clim.*, *16*, 3706–3722.

Trenberth, K. E., and Stepaniak (2004), The flow of energy through the Earth's climate system, *Q. J. R. Metereol. Soc.*, *130*(Part B), 2677–2701.

Trenberth, K. E., J. M. Caron, and D. P. Stepaniak (2001), The atmospheric energy budget and implications for surface fluxes and ocean heat transports, *Clim. Dyn.*, *17*, 259–276.

Trenberth, K. E., J. Fasullo, and L. Smith (2005), Trends and variability in column-integrated water vapor, *Clim. Dyn.*, *24*, 741–758.

Uppala, S. M., et al. (2005), The ERA-40 reanalysis, *Q. J. R. Meteorol. Soc.*, *131*, 2961–3012.

Vinje, T. (2001), Fram Strait ice fluxes and atmospheric circulation: 1950–2000, *J. Clim.*, *14*, 3508–3517.

Vinje, T., N. Nordlund, and A. Kvarnbekk (1998), Monitoring ice thickness in Fram Strait, *J. Geophys. Res.*, *103*, 10437–10449.

Woodgate, R. A., K. Aagaard, and T. L. Weingartner (2006), Interannual changes in the Bering Strait fluxes of volume, heat and freshwater between 1991 and 2004, *Geophys. Res. Lett.*, *33*, L15609, doi:10.1029/2006GL026931.

Yang, S.-K., Y.-T. Hou, A. J. Miller, and K. A. Campana (1999), Evaluation of the Earth radiation budget in the NCEP-NCAR reanalysis with ERBE, *J. Clim.*, *12*, 477–493.

Zhang, J. (2005), Warming of the arctic ice-ocean system is faster than the global average since the 1960s, *Geophys. Res. Lett.*, *32*, L19602, doi:10.1029/2005GL002416.

Zhang, J., and D. A. Rothrock (2003), Modeling global sea ice with a thickness and enthalpy distribution model in generalized curvilinear coordinates, *Mon. Weather Rev.*, *131*, 681–697.

Zhang, T., et al. (2005), Spatial and temporal variability in active layer thickness over the Russian Arctic drainage basin, *J. Geophys. Res.*, *110*, D16101, doi:10.1029/2004JD005642.

A. P. Barrett, M. C. Serreze, and A. G. Slater, Cooperative Institute for Research in Environmental Sciences, University of Colorado, Boulder, CO, USA. (serreze@kryos.colorado.edu)

M. Steele and J. Zhang, Applied Physics Laboratory, Polar Science Center, University of Washington, Seattle, WA, USA.

K. E. Trenberth, National Center for Atmospheric Research, Boulder, CO, USA.